

Thorough small-angle X-ray scattering analysis of the instability of liquid micro-jets in air

Benedetta Marmiroli,^{a*} Fernando Cacho-Nerin,^{a‡} Barbara Sartori,^a Javier Pérez^b and Heinz Amenitsch^{a*}

^aInstitute of Inorganic Chemistry, Graz University of Technology, Stremayrgasse 9/IV, Graz 8010, Austria, and ^bBeamline SWING, Synchrotron SOLEIL, L'Orme des Merisiers, Saint-Aubin, BP 48, 91192 Gif sur Yvette, France. *E-mail: benedetta.marmiroli@tugraz.at, heinz.amenitsch@tugraz.at

Liquid jets are of interest, both for their industrial relevance and for scientific applications (more important, in particular for X-rays, after the advent of free-electron lasers that require liquid jets as sample carrier). Instability mechanisms have been described theoretically and by numerical simulation, but confirmed by few experimental techniques. In fact, these are mainly based on cameras, which is limited by the imaging resolution, and on light scattering, which is hindered by absorption, reflection, Mie scattering and multiple scattering due to complex air/liquid interfaces during jet break-up. In this communication it is demonstrated that synchrotron small-angle X-ray scattering (SAXS) can give quantitative information on liquid jet dynamics at the nanoscale, by detecting time-dependent morphology and break-up length. Jets ejected from circular tubes of different diameters (100–450 μm) and speeds (0.7–21 m s^{-1}) have been explored to cover the Rayleigh and first wind-induced regimes. Various solvents (water, ethanol, 2-propanol) and their mixtures have been examined. The determination of the liquid jet behaviour becomes essential, as it provides background data in subsequent studies of chemical and biological reactions using SAXS or X-ray diffraction based on synchrotron radiation and free-electron lasers.

Keywords: SAXS; free liquid micro-jet; break-up length; jet instability; refraction; liquid mixtures.

© 2014 International Union of Crystallography

1. Introduction

Liquid jets are exploited in many industrial areas. For example, they can be found in engines as fuel injectors, in ink-jet printing, in spray-drying of food and pharmaceutical ingredients. They have also been employed in scientific investigations like mass spectrometry (Stengel *et al.*, 2012), photoelectron spectroscopy (Suzuki, 2012), X-ray absorption and emission (Wilson *et al.*, 2002; Lange *et al.*, 2010), and X-ray diffraction (XRD) (Priebe *et al.*, 2010). Interest has further increased due to the evolution of free-electron lasers (FELs) and the consequent need to develop new high-throughput techniques, *i.e.* to characterize biological macromolecules (Spence *et al.*, 2012). For this purpose, liquid jets have been tailored for X-ray FEL radiation to convey samples in a continuous way in order to avoid radiation damage (Shapiro *et al.*, 2008; Priebe *et al.*, 2010; Chapman *et al.*, 2011; Boutet *et al.*, 2012; Redecke *et al.*, 2013). These pilot studies have demonstrated the potential for structural investigation of chemical

and biological reactions. All these applications demand knowledge of the temporal and spatial evolution of the liquid jet (Sander & Weigand, 2008).

Liquid jet break-up has been intensely described both by theoretical analyses and numerical simulations, the latter gaining importance with the improvement of the numerical methods to follow the free surface. An in-depth overview has recently been dedicated to liquid jet break-up (Eggers & Villermaux, 2008).

Experimental data sets describing the jet behaviour and allowing a comparison with theoretical predictions and numerical simulations are still incomplete.

Various experimental techniques have been employed to analyze jet fragmentation: stroboscopic illumination of the jet and laser photometry methods (Kalaaji *et al.*, 2003), ultra-high-speed imaging (van Hoeve *et al.*, 2010), environmental scanning electron microscopy (Deponte *et al.*, 2009) and environmental field-emission transmission electron microscopy (Deponte *et al.*, 2011), to cite only a few. However, it is still very difficult to characterize the phenomena of physical instabilities developing in the transition zone between the

[‡] Current address: Diamond Light Source, Harwell Science and Innovation Campus, Didcot OX11 0DE, UK.

liquid jet and the spray due to the presence of many interfacial scales (Delteil *et al.*, 2011).

In fact, as shown in the previous examples, most experimental techniques are based on camera imaging which has a limit in the minimum detectable length scale of the phenomena, and on light scattering which is affected by absorption, refraction/reflection, Mie scattering and multiple scattering of droplets and of the morphology at the air/liquid interface.

Synchrotron small-angle X-ray scattering (SAXS) can overcome some of these limitations. It is considered a standard method to characterize nanostructures in the dimensional range 1–100 nm (Feigin & Svergun, 1987). Even if microscopy techniques like SEM and TEM can reach this structural scale, SAXS generally allows a more versatile sample environment. More importantly, time-resolved *in situ* studies can be easily performed, while detailed information averaged over the irradiated sample volume and over the exposure time can be obtained (Amenitsch & Marmioli, 2011). In the study of liquid jets, this represents a further advantage, as this kind of measurement is effective for examining surface roughness and droplets.

SAXS and XRD have already been employed in combination with liquid jets to study evolving chemical reactions with high time resolution (Haberkorn *et al.*, 2003; Marmioli *et al.*, 2009; Schmidt *et al.*, 2010; Polte *et al.*, 2010). Measuring the jet at increasing distance from the nozzle is equivalent to measuring at increasing time from the beginning of the reaction. In a previous work (Marmioli *et al.*, 2009) we have reported a micromixer producing a free liquid jet in air to study the early stages of chemical and biological reactions with SAXS. After devising a method to align the jet with the X-ray beam with a resolution better than 20 μm (Marmioli *et al.*, 2010), we examined the formation of calcium carbonate nanoparticles starting from 100 μs . We stated that the induction time of the reaction was less than 200 μs , but during subsequent experiments we found that the SAXS signal of the liquid jet itself could be detected, casting doubts on the nature of the phenomenon occurring at 200 μs . In order to deepen our understanding of the jet functioning, we decided to conduct a thorough SAXS investigation. This knowledge will allow us to subtract the SAXS signal produced by the jet in subsequent measurements of biological and chemical reactions using the micromixer.

In the present communication the effectiveness of synchrotron SAXS in providing quantitative information on the dynamics of liquid jets at the nanoscale is shown. Liquids ejected in still air from circular holes of different diameters, jet speed and solvents have been studied. The time-dependent morphology and their break-up length have been determined.

2. Theory

Independently of their flow conditions and environment, all liquid jets break, *i.e.* the continuous stream becomes fragmented into droplets. The physical mechanism leading to disintegration of a liquid injected into vacuum or in a gaseous

environment is mainly caused by the character of the nozzle flow and, in the second case, also by the aerodynamic interaction between the two fluids. At low speed the fluid drips from the nozzle. As the flow rate increases, the jet builds up. There are different break-up modes as a function of jet speed. The first is the Rayleigh break-up mode, studied since the nineteenth century by Plateau, Rayleigh and Weber (Rayleigh, 1879). It leads to drop formation whose dimensions are larger than the jet diameter. Interface tensions between the liquid and the surrounding gas amplify small perturbations (capillary instability) introduced by mechanical vibrations or by thermal fluctuations. These perturbations propagate along the interface as surface waves of specific amplitude and wavelength. The amplification of the capillary instability induces the break-up of the jet.

When the flow rate increases, the relative velocity between the jet and the ambient air can no longer be neglected; aerodynamic effects appear and generate a shear at the interface between the fluids that accelerate the break-up process and shorten the distance from the nozzle exit to the location of droplet pinch-off. The break-up of the jet into droplets is given by a coupling between capillary instability caused by the surface tension and a Kelvin–Helmholtz instability typical of sheared flows. This is called the *first wind-induced* break-up. By further increasing the jet speed, inertia effects increase and the jet enters the so-called *second wind-induced regime*. The flow becomes turbulent and disintegration takes place near the nozzle. By increasing the flow rate, the *atomization* regime is finally reached where the droplets form at the nozzle exit (van Hoeve *et al.*, 2010; Delteil *et al.*, 2011).

The jet can be described with several geometrical and physical values which define the nozzle geometry (among which nozzle diameter D), the flow field (bulk inflow velocity V_0) and the physical properties of the fluid (density ρ , dynamic viscosity μ and kinematic viscosity $\nu = \mu/\rho$, surface tension γ). For a practical description of jet break-up, it is convenient to use the *break-up length* L_b , defined as the intact length of the jet that is the distance from the nozzle at which the jet becomes a spray. This magnitude can be made dimensionless in the so-called *dimensionless break-up length* L_b^* , which is the ratio between the break-up length L_b and the initial diameter D .

Since the important physical mechanisms during the primary break-up process are related to the flow characteristics as well as to the nozzle geometry and to the fluid properties, the break-up regime can be identified by the following dimensionless numbers:

Reynolds number, representing the ratio of inertial and viscous forces, $\text{Re} = \rho V_0 D / \mu$;

Weber number, representing the ratio of inertia and surface tension forces, $\text{We} = \rho V_0^2 D / \gamma$;

Ohnesorge number, representing the ratio of damping viscous forces and surface tension forces, $\text{Oh} = \sqrt{\text{We}} / \text{Re}$.

Gravitational effects are neglected.

If the fluid viscosity is also neglected and the Rayleigh break-up region is considered, a characteristic timescale of the

motion is described by the characteristic time or capillary time, $\tau = (\rho R_0^3 / \gamma)^{1/2}$, where R_0 is the initial radius of the fluid cylinder. τ is related to the total time for break-up to occur. It is the time that it takes for the surface wave caused by perturbations to reach an amplitude equal to R_0 .

Many criteria have been proposed to determine the range of each break-up mode occurrence and more particularly for the Rayleigh break-up regime. For a given system (combination of fluid, geometry and environment), L_b depends on the jet speed V_0 , as depicted in Fig. 1(a). After the jet dripping regime, L_b increases monotonically with speed up to a maximum value. Then L_b decreases with speed, entering the wind-induced regimes and ending in atomization, where it becomes undefined (Lin & Reitz, 1998). An alternative representation of this classification is the Ohnesorge–Miesse diagram, which represents these regimes as regions in the Re–Oh plot (see Fig. 1b) (Sander & Weigand, 2008).

Goldin *et al.* (1969) proposed a semi-empirical equation to correlate the dimensionless break-up length L_b^* in Rayleigh break-up with the Weber and Reynolds numbers,

$$L_b^* = C [(We)^{1/2} + 3(We/Re)], \quad (1)$$

where C is a constant that depends on the initial magnitude of the disturbance, and is determined experimentally.

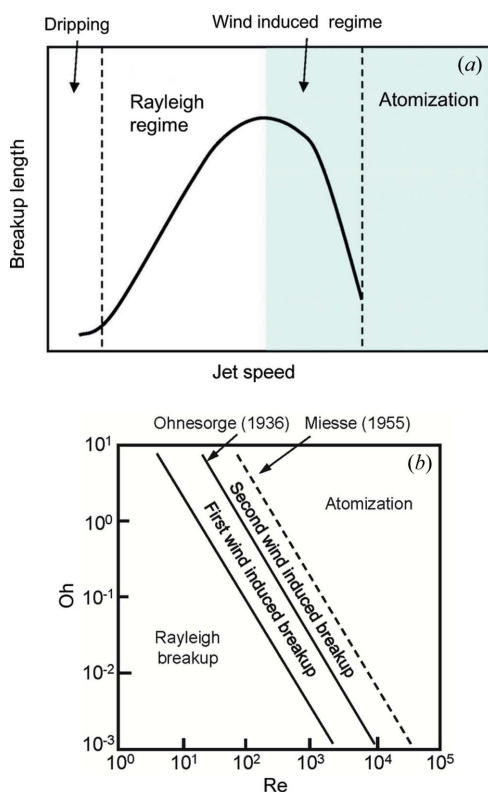


Figure 1
(a) Schematic diagram of break-up modes represented by break-up length as a function of jet speed (Lin & Reitz, 1998). (b) Schematic diagram of break-up modes based on the criteria of Ohnesorge and Miesse (Sander & Weigand, 2008).

3. Experimental

3.1. Set-up

While most experimental studies examine the behaviour of free jets in air under controlled stimulation to avoid random events, the present measurements have been performed on a jet subjected only to ‘natural’ break-up, for instance caused by casual perturbations at the nozzle.

The SAXS measurement has been conducted using the experimental set-up described in the following (detail shown in Fig. 2a). The free jet exits from a stainless steel pipe with a circular hole which is connected to a high-pressure syringe pump (Model 500D, Teledyne ISCO, Lincoln, NE, USA). The jet evolution is studied through a snake-like scan along the liquid stream at increasing distance from the nozzle exit, therefore probing increasing times. The scan is performed by moving the stainless steel tube with respect to the X-ray beam. Time resolution is only limited by the dimension of the X-ray beam. The advantage of this method is that there is no need of ultrafast detectors as the liquid in the same place is always under the same conditions.

SAXS measurements have been conducted using a photon energy of 8 keV both at the Austrian SAXS beamline (Amenitsch *et al.*, 1998) at Elettra Synchrotron in Italy and at the SWING beamline (David & Pérez, 2009) at Soleil Synchrotron in France. For the experiments conducted at Elettra, the X-ray beam was adjusted to dimensions of 0.2 mm width and 0.9 mm height. A two-dimensional pixel detector (Pilatus 100k, Dectris) has been used to record the SAXS patterns. The detector covered the scattering vector q -range from about 0.1 to 2.6 nm^{-1} . For the experiments conducted at Soleil the beam was adjusted to dimensions of 0.325 mm width and 0.075 mm height, to obtain a higher spatial resolution. A two-dimensional CCD detector in vacuum (AVIEX170170)

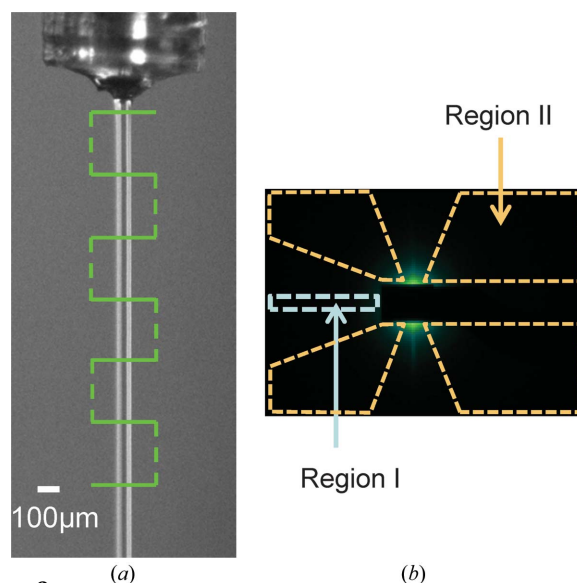


Figure 2
(a) Tube and free water jet in air ($100 \mu\text{m}$ diameter, 4.7 m s^{-1} speed) with a scheme of the scan in a snake-like mode. (b) Schematic scattering pattern with the two masks corresponding to two different regions (refraction I and scattering II) used for data analysis.

has been used to record the SAXS patterns, covering a q -range from about 0.05 to 4.2 nm^{-1} . In both cases the q -scale of the diffraction pattern has been calibrated with silver behenate (Lu *et al.*, 2001) [$q = 4\pi/\lambda \sin(\theta/2)$, with λ the X-ray wavelength and θ the scattering angle]. The sample holder was connected to an XY translation stage with micrometer precision.

3.2. Experimental conditions

Jets produced by three stainless steel tubes with different diameters (100 μm , 250 μm , 450 μm) have been investigated. Micrographs of the three tubes' openings are shown in Fig. S1 of the supporting information.¹

Diverse fluids have been examined: water, ethanol, 2-propanol (IPA), a mixture of ethanol and water 50% in volume, and a mixture of IPA and water 50% in volume. Water was of Milli-Q quality, absolute ethanol (99.9%) was purchased from Roth GmbH, and pure IPA (99.7%) from J. T. Baker (Mallinckrodt Baker).

The fluid characteristics at 298 K, taken from the literature (Chu & Thompson, 1962; Vazquez *et al.*, 1995; El-Banna & Ramadan, 1995; Pires *et al.*, 2007), are summarized in Table 1.

The fluids have been pumped at increasing flow rates chosen to cover the Rayleigh and first wind-induced regime, as shown in the Ohnesorge–Miesse diagram in Fig. 7(a): 2.235 ml min^{-1} , 4.47 ml min^{-1} , 6.67 ml min^{-1} , 10 ml min^{-1} . The corresponding jet speed at the nozzle exits is in the range 0.7–21 m s^{-1} , the Reynolds number in the range 200–2600, and the Weber number in the range 2–800. Therefore, the fluid inside the tube changes from laminar to transition regime at the highest speed. The experiments have been repeated, in order to measure a statistically relevant break-up. A summary of the experimental conditions and of the related dimensionless numbers is reported in Table 2.

3.3. Data treatment

The two-dimensional patterns have been integrated after geometric corrections using the program *Fit2D* (Hammersley,

Table 1
Liquid parameters at 298 K.

	Surface tension (N m^{-1})	Density (kg m^{-3})	Kinematic viscosity ($\text{m}^2 \text{ s}^{-1}$)
Water	0.072	997.0479	8.92×10^{-7}
Ethanol	0.02182	785.2	1.38×10^{-6}
IPA	0.02122	785	2.54×10^{-6}
Ethanol–water 50%v	0.03016	923	2.54×10^{-6}
IPA–water 50%v	0.02527	925.8	3.45×10^{-6}

¹ Supporting information for this paper is available from the IUCr electronic archives (Reference: CO5047).

Table 2
Summary of the experimental parameters of the jet.

	Jet speed (m s^{-1})	Reynolds number	Weber number	Ohnesorge number	Characteristic time (s)
Water	0.7–21.2	212–2390	2–624	4.95×10^{-3} – 1.05×10^{-2}	4.16×10^{-5} – 3.97×10^{-4}
Ethanol	0.7–14.2	137–1720	5–810	1.23×10^{-2} – 3.62×10^{-2}	6.7×10^{-5} – 6.4×10^{-4}
IPA	0.7–14.2	75–935	5–832	2.3×10^{-2} – 4.89×10^{-2}	6.8×10^{-5} – 6.5×10^{-4}
Ethanol–water 50%v	1–14.2	187–935	15–689	2.09×10^{-2} – 4.44×10^{-2}	6.18×10^{-5} – 5.9×10^{-4}
IPA–water 50%v	1–14.2	114–686	18–824	3.12×10^{-2} – 6.6×10^{-2}	6.76×10^{-5} – 6.46×10^{-4}

1998) with two different masks. Mask I corresponds to the refraction/reflection region of the undisturbed jet, and mask II is related to the scattering region of the jet. Both regions are shown in Fig. 2(b).

In order to visualize the evolution of the studied jet, the integrated intensity \tilde{I} has been calculated using the following expression (Porod, 1952) in which $I(q)$ is the intensity at the detector,

$$\tilde{I} = \int I(q) dq. \tag{2}$$

\tilde{I} has been determined separately for region I and for region II. Region I was defined specifically for each experiment to cover only the refraction streak.

The dominant effect of the measured scattering intensity I , due to the used X-ray wavelength, the dimensions of the jet and of the droplets after break-up ($>10 \mu\text{m}$), is given by the total reflection and refraction from their geometrical form. A sketch of the X-ray deflection of circular objects by refraction and total reflection, and the angular intensity distribution for cylinders and spheres adapted from Hentschel *et al.* (1987), are shown in Fig. 3 where δ is the critical angle. For $\theta < 2\delta$ the contribution of the refraction is predominant with respect to that of reflection.

The approximate equations for refraction from a cylinder are given by Hentschel *et al.* (1987) and the exact solution by Amenitsch (1992) using a Heaviside function as simplified transmission/reflection curve. An equivalent approximated solution for the cylinder was also calculated by Plomp *et al.* (2007). The equation given by Plomp *et al.* (2007) is

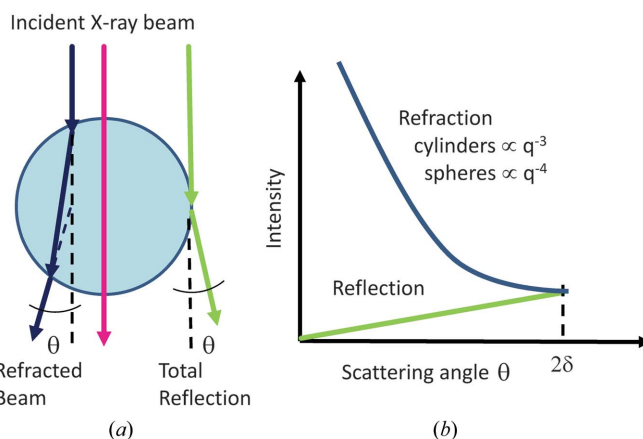


Figure 3
(a) Sketch of the X-ray refraction and total reflection from circular objects. (b) Intensity distribution as a function of the scattering angle for cylinders and spheres according to Hentschel *et al.* (1987).

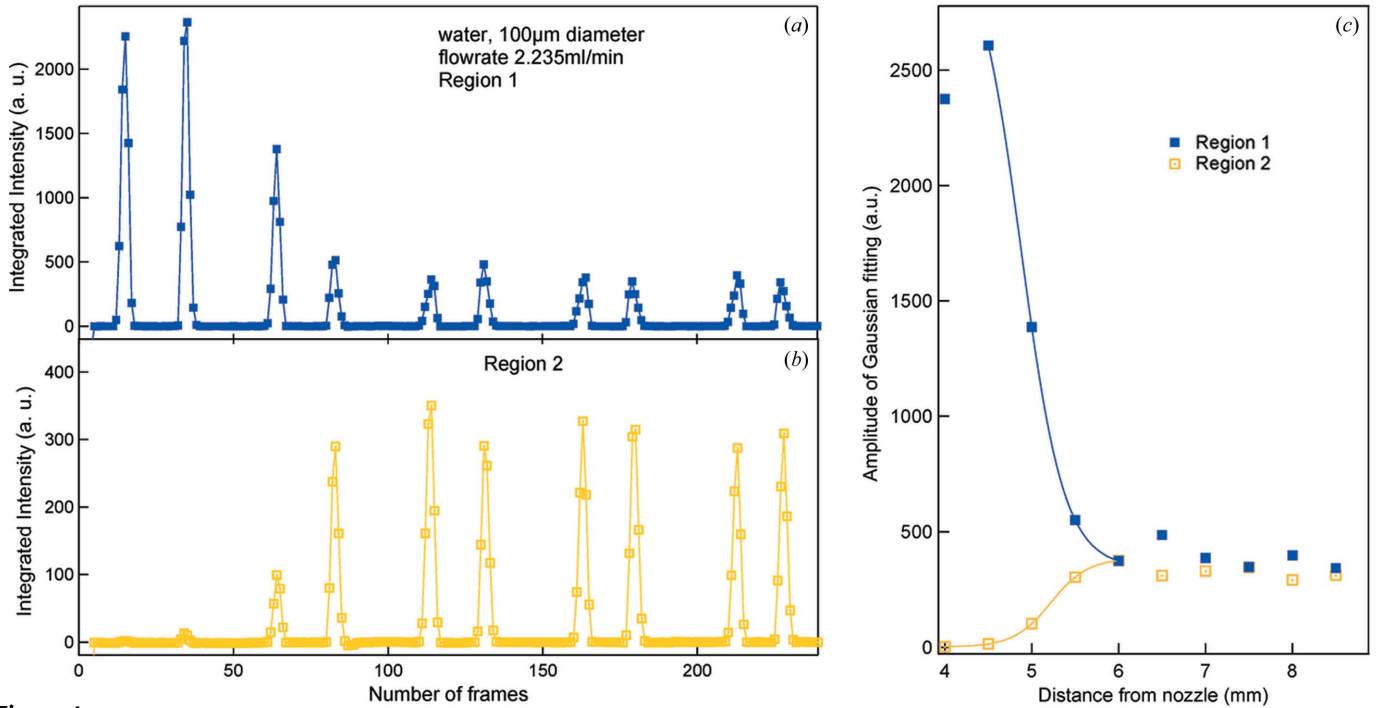


Figure 4 (a) Integrated intensity *versus* number of acquired frames for a snake-like scan of a water jet of initial diameter 100 μm with a flow rate of 2.235 ml min^{-1} referred to region I. (b) Integrated intensity *versus* number of acquired frames for the same scan, but calculated for region II. (c) Amplitude of the Gaussian fitting of the integrated intensity *versus* distance from the nozzle for the water jet for regions I and II. The points are fitted with a sigmoid curve (shown in the picture) whose position of half value is considered as the jet break-up length.

$$I_r(\theta) = \frac{I_0 R_{\text{cyl}}}{2\varepsilon} \frac{1}{[1 + (\theta/2\varepsilon)^2]^{3/2}}. \quad (3)$$

The equation is valid for $\theta < 2\delta$ where $\delta = \sqrt{2}\varepsilon$ is the critical angle and ε is the refractive index decrement ($n = 1 - \varepsilon$). I_0 is the intensity per unit length, and R_{cyl} the dimension of the cylinder. The transmission coefficients and the absorption in the jet have been neglected. The behaviour for $\theta < 2\delta$ and the asymptotic behaviour for large scattering angles $\theta \gg \varepsilon$ can be approximated with

$$I_r(q) \propto 1/q^3. \quad (4)$$

The contribution of the total reflection from a cylinder can be calculated with

$$I_{\text{tr}}(\theta) = I_0 R_{\text{cyl}} 2 \sin(\theta/2) R_f(\theta/2). \quad (5)$$

In (5) the Fresnel reflectivity $R_f(\theta/2)$ has been introduced additionally with respect to the original literature (Hentschel *et al.*, 1987).

The regime of the total reflection is limited to the small layers at the outer parts of the cylinder Δ , which can be estimated by the formula (Hentschel *et al.*, 1987)²

$$\Delta = 2 R_{\text{cyl}} [1 - \cos(\delta)] \simeq 2 \varepsilon R_{\text{cyl}}. \quad (6)$$

Equation (3) can be expanded to the isotropic case, *i.e.* droplets considered as spheres under the same approxima-

tions, by calculating the isotropic differential scattering cross section,

$$I_r(\theta) = j_0 R^2 \frac{1}{2\varepsilon} \frac{1}{[1 + (\theta/2\varepsilon)^2]^2}, \quad (7)$$

where j_0 is the photon flux density and R the radius of the droplets. The behaviour for $\theta < 2\delta$ and the asymptotic behaviour for large scattering angles $\theta \gg \varepsilon$ can be approximated with

$$I_r(q) \propto 1/q^4, \quad (8)$$

which is equivalent to the equation given by Hentschel *et al.* (1987).

4. Results and discussion

An example of results from the SAXS measurements of the snake-like scan are shown in Figs. 4(a) and 4(b), in which the integrated intensity \bar{I} has been plotted as a function of the number of acquired frames for both the region I and II for a water jet exiting from a circular nozzle with diameter 100 μm and flow rate 2.235 ml min^{-1} . Due to the continuous snake-like scan, the intensity distribution of every peak is given by the convolution of the X-ray beam profile with the moving jet during each exposure. The parameters have been set to achieve a sampling distance of 200 μm between each exposure in the horizontal part of the scan, and of 500 μm in the vertical part. From the graphs, the evolution of the jet morphology is evident from the change in the peak heights. Moreover, the

² Note that even though it was not mentioned in the text of the original literature, the effects of the influence of the reflectivity have been discussed in the figure of total reflection.

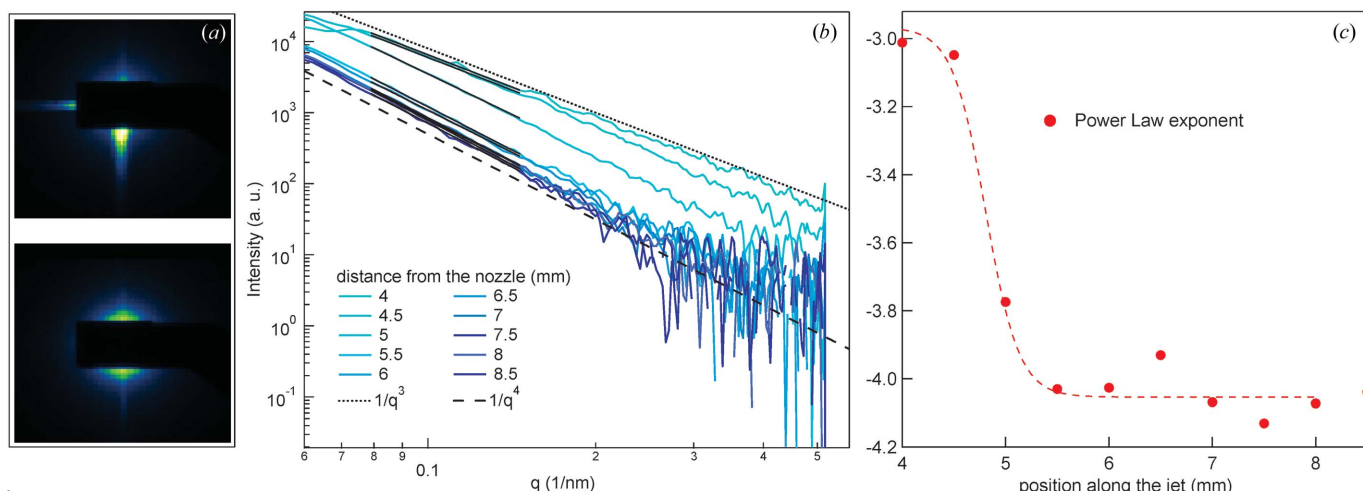


Figure 5 (a, top) Diffraction pattern of a water jet with initial diameter $100\ \mu\text{m}$ and flow rate $2.235\ \text{ml}\ \text{min}^{-1}$ before the onset of jet instability [peak 1 of Fig. 4(a)] and (a, bottom) after the onset of jet instability [peak 7 of Fig. 4(a)]. (b) Scattering patterns of region I for a water jet exiting from a circular nozzle with diameter $100\ \mu\text{m}$ and flow rate $2.235\ \text{ml}\ \text{min}^{-1}$ at the maxima of the integrated intensity of Fig. 4(a). The continuous lines represent the fitting results of a power law onto the data. The upper dotted line is the theoretical curve for the refraction from a cylinder [equation (4)]. The lower dotted curve represents the theoretical curve for the refraction from spheres [equation (8)]. (c) Power law exponent as a function of the position along the jet showing the change from the refraction contribution of a cylinder to that of a droplet. The dotted line is a guide for the eye.

position of the first peaks of region I is slightly shifted with respect to those of region II which is due to the different contributions: the refraction of the unperturbed jet is higher at the jet interface (region I), while the main contribution to region II is the scattering of the jet. Each peak has been fitted with a Gaussian curve, and the respective heights of the Gaussian have been reported as a function of the distance from the nozzle, as shown in Fig. 4(c) for region I and II.

Region I is related to the scattering/refraction phenomena perpendicular to the jet axis. The diffraction pattern from the jet immediately adjacent to the tip shows a sharp horizontal streak (equatorial plane) in region I due to the X-rays refracted from the cylindrical jet’s geometry, which is predicted by refraction theory and visible in Fig. 5(a) (top). The high values of intensity give a strong contribution to the integrated intensity \bar{I} of region I that then decreases its value as soon as the jet starts to break up and droplets appear. The change of refraction from the equatorial to the isotropic refraction (droplets), as evident in Fig. 5(a) (bottom), is the reason behind this. The same effect with an opposite trend is observable in the integrated intensity of region II. There, the integrated intensity is roughly zero, due to the isotropic weak scattering of water in the jet, then sharply increases reaching a maximum, and remains at higher values with small fluctuations in the same level as the signal from region I. A similar behaviour was phenomenologically described by Shapiro *et al.* (2008).

To gain further insight into jet instability, simulations of the reflection and refraction pattern have been performed and the results are shown in Fig. 6. The simulation of the refraction follows the approximated behaviour of equation (3) up to the critical angle, neglecting the transmission coefficients between the air/water interface as well as of the absorption in the water.

The contribution of total reflection leads to the formation of a shoulder at the critical angle, *i.e.* at a scattering vector of

$0.22\ \text{nm}^{-1}$, where the reflection should be of the order of the refraction contribution according to the theory [equation (5)]. This shoulder has not been observed in the present experiments. This has been attributed to the fact that, with the jet diameters used in our experiment, the reflection layer Δ is of the order of $3\ \text{nm}$. Therefore contributions of capillary waves and intrinsic roughness at the liquid/air interface become important, which are not included in the theory of Hentschel *et al.* (1987) based on a flat surface on the nanoscopic scale. The region in which the deviation from the ideal power law behaviour of the refraction described in equations (4) and (8) occurs has been estimated in the range $2\delta - 10\varepsilon < \theta < 6\delta$. The lower limit is given by the deviation from the power law due to neglecting the transmission coefficients and water absorption, and the upper limit is given by the asymptotic power law behaviour of the reflectivity curve for grazing angles larger

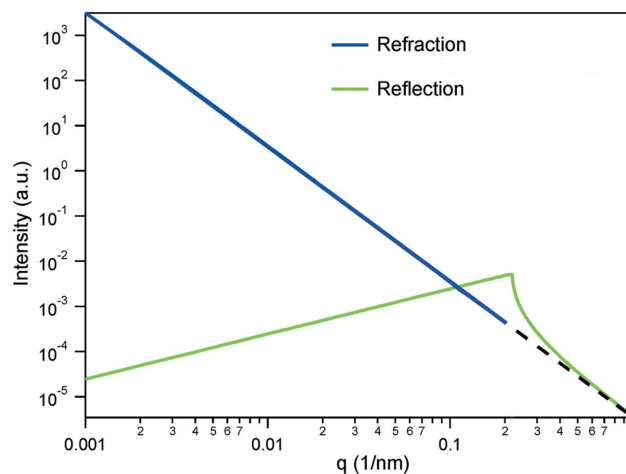


Figure 6 Simulations of the reflection and refraction pattern for a water jet of $100\ \mu\text{m}$ diameter following equations (3) and (5).

than three times the critical angle (Tolan, 1999). These limits are about 0.12 and 0.6 nm^{-1} in the case of water.

SAXS patterns for region I are reported in Figs. 5(b) and 5(c) for the water jet exiting from the circular nozzle with diameter $100 \mu\text{m}$ and flow rate $2.235 \text{ ml min}^{-1}$. The curves in Fig. 5(b) correspond to the peak positions in Fig. 4(a), taken at increasing distance from the tube exit. They have been fitted by a general power law following equations (4) and (8) valid for q values smaller than 0.12 nm^{-1} . The fitting results in terms of power law exponent are shown in Fig. 5(c) as a function of the position along the jet. It can be seen that there is a change from the value -3 , the refraction of a cylinder at the position of the unperturbed jet, to the value -4 , the refraction of a droplet after the jet break-up as expected by the theory for the changing geometry. For a detailed investigation of jet scattering for the extreme cases before and after the jet break-up, see the supporting information (Fig. S2), in which the results of the horizontal scan are shown and in which it is demonstrated that the power law is independent of the horizontal position.

The oscillations of the integrated intensity, Fig. 4(c), are explained by the oscillatory changes of droplet shapes after break-up from oblate to prolate and *vice versa*, as shown in the high-speed images around the jet break-up in the supporting information (see Fig. S4). In fact, the break-up has also been measured for the $100 \mu\text{m}$ -diameter water jet at $2.235 \text{ ml min}^{-1}$ in the Rayleigh regime by using a high magnification and high-speed camera (FASTEC HISPEC, FASTEC Imaging, San Diego, CA, USA). The video is shown in the supporting information. The length scale of 1 mm for this oscillatory effect in the high-speed images fits well to the length scale of the observed oscillations determined from the integrated intensities in SAXS (Fig. 4c). Also, the expected anti-phase appearance of the integrated intensity in the regions I and II is observed, as oblate particles with reference to the axis refract stronger in the vertical (region II) than in the horizontal (region I). For prolate particles the opposite is valid.

We associate the growth of the integrated intensity with the onset of jet instability and subsequent break-up. For the determination of the break-up length, the integrated intensity corresponding to the peaks as a function of the position along the jet has been fitted with a sigmoid function. The position of the half-width has been considered the break-up length (Fig. 4c). The break-up time has then been defined as the break-up length divided by the jet speed at the tube exit.

The determination of the break-up length is limited by the error introduced by the finite dimension of the height of the X-ray beam: the smaller the beam, the smaller the error.

Sources of error are related to the dynamic character of the surface tension, to the evolution of the velocity profile along the jet, to the contraction of the cross section due to the complex hydrodynamics near the nozzle opening, to the non-linear growth of the perturbation, and to the non-linearity of excitation. These perturbations affect both jet diameter and speed, thus leading to uncertainties in the value of the break-up time. In the present paper such effects have been neglected.

The break-up length as a function of jet speed at the nozzle exit has been plotted for all the tested conditions, as shown in Fig. 7(b). It can be noticed that such curves follow the behaviour predicted by Fig. 7(a). In fact, the points corresponding to the first wind-induced regime of the Ohnesorge–Miesse diagram fall in the wind-induced area also in this second graph, as they present values that are equal or below the maximum. Our assumption to define the break-up length is still proved correct. The break-up length values measured for the $100 \mu\text{m}$ -diameter water jet at $2.235 \text{ ml min}^{-1}$ have also been confirmed by the images taken with the high-speed camera.

In Fig. 7(b) the dependence of the break-up length on jet diameter is also highlighted. When the jet speed at the tube exit is the same, the smaller the jet radius then the shorter its break-up length. Moreover, different liquids present different break-up length if produced under the same conditions (diameter of the tube and flow rate). In particular, ethanol and IPA have a higher break-up length than water. Such results,

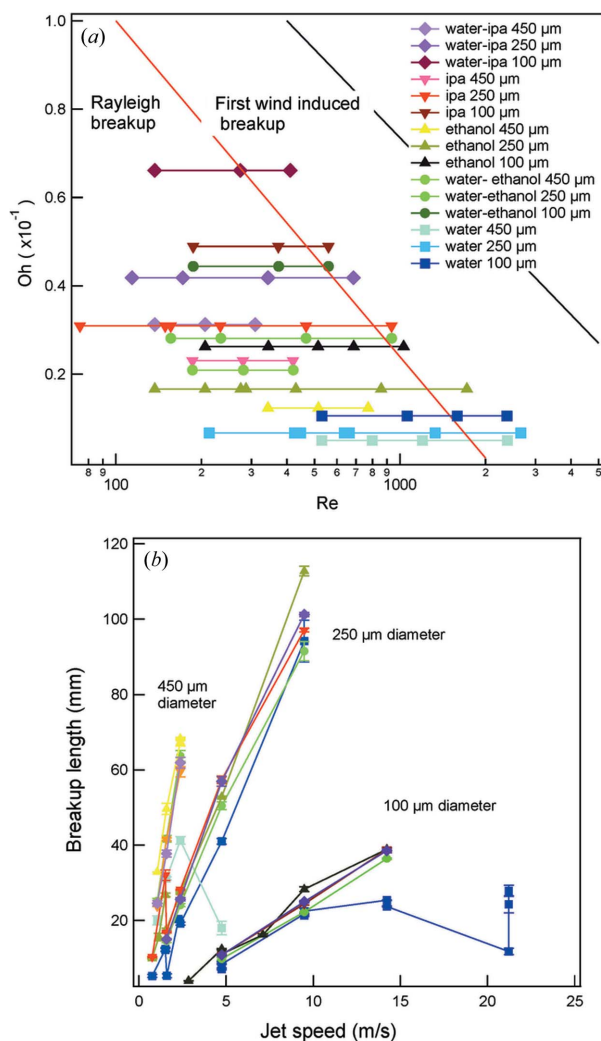


Figure 7 (a) Ohnesorge–Miesse diagram for the employed experimental conditions. (b) Break-up length versus jet speed at the nozzle exit for all the performed tests. All the lines between the points are drawn as a guide for the eye.

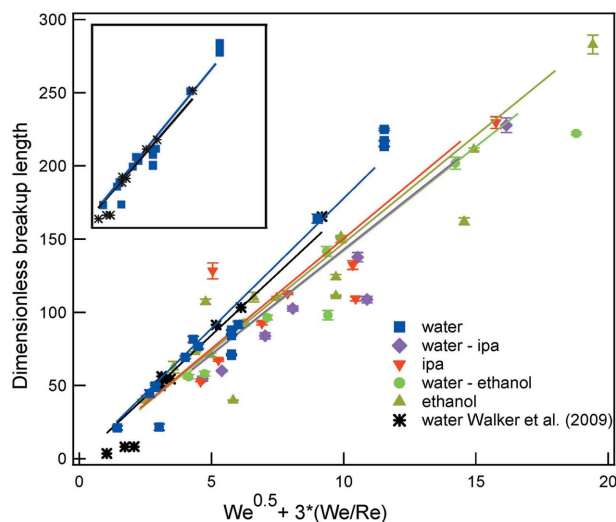
that may appear trivial to the fluid dynamics experts, nonetheless demonstrate that our method to define the break-up length is both robust and consistent with experiments conducted by high-speed imaging and predicted by theory. This is even confirmed in the case of water mixtures with ethanol or with IPA (shown in Fig. S5 of the supporting information). In fact, the behaviour of the mixtures is more similar to that of ethanol and IPA, respectively. The surface tension values of the mixtures, shown in Table 1, are next to ethanol and IPA rather than to water. This is in agreement with the ideas expressed by Homer *et al.* (2009) and Innocenzi *et al.* (2008) for droplets: the liquids with lower surface tension tend to migrate at the surface of the droplets and to evaporate first.

In fact, initially, alcohol evaporates more rapidly from the surface giving rise to a concentration gradient within the droplet. In the present case, the respective depletion of ethanol and IPA from the surface of the jet would be higher than that of water, therefore driving the break-up process. This also demonstrates the complexity of the break-up processes for liquid jets undergoing chemical reactions. It becomes essential to use the jet signal as background for the following measurements. Moreover, the experiment has to be conducted under conditions close to the real ones of the chemical reaction being investigated.

As already stated, the presence of many parameters involved in the description of liquid jets leads to the definition of dimensionless numbers in order to limit the amount of variables. Fig. 8 shows the dimensionless break-up length as a function of the second term of the Goldin equation (1) for all the liquids studied in the Rayleigh break-up range. The value of the constant *C* has been determined for every liquid with a small error. Again, the slope of equation (1) in the case of mixtures is more similar to the value of the respective alcohols than to water. The inset of Fig. 8 shows a comparison of the data obtained in the present experiments with those gathered from a free liquid jet in air measured by Walker *et al.* (Walker & Calabrese, 2011; Walker, 2012) using a high magnification and high-speed camera. It can be seen that our value of *C*, 17.3, is very similar to that of the reference, 16.9.

In Fig. 9 the dimensionless break-up time is reported as a function of the jet speed for every fluid in the Rayleigh regime. We defined the dimensionless break-up time as the ratio of the experimental break-up time and the characteristic time. By making an average of all the values, the dimensionless break-up time is equal to 42.9 with an average deviation of ± 5.7 . In other words, the break-up time is around 43 times the characteristic time, and, when designing an experiment, it is possible to estimate the break-up time of most common solvents in the Rayleigh regime *a priori* by calculating the characteristic time.

The present data have been obtained for tubes with inner diameters in the 100–450 μm range. The inner tubes of the devices producing jets for FEL experiments are in the 20–50 μm range. The liquid jet exiting the tube is then focused with a co-flowing gas stream to reach a liquid jet with even smaller diameter. From the literature (van Hoeve *et al.*, 2010)



Fluid	<i>C</i>	<i>C sigma</i>
Water	17.3	± 0.6
Water-IPA	12.7	± 0.6
IPA	13.7	± 1.0
Water-Ethanol	12.9	± 0.6
Ethanol	13.8	± 0.6
* Water (Walker, C.)	16.9	± 0.9

Figure 8 Dimensionless break-up length as a function of the second term of equation (1) for all the examined liquids in the Rayleigh break-up range. All data have been fitted with a line, allowing the determination of *C*, reported in the table. In the inset, a comparison between SAXS data for water and data collected by Walker *et al.* (Walker & Calabrese, 2011; Walker, 2012) with a camera is shown.

it can be deduced that the Rayleigh instability causes break-up of microscale liquid jets in the same ways as in the macro scale. However, the mode of operation with the co-flowing gas distinguishes FEL jets from our case, so that parameters for FEL operation cannot be readily extrapolated from the present work. Specific experiments should be conducted

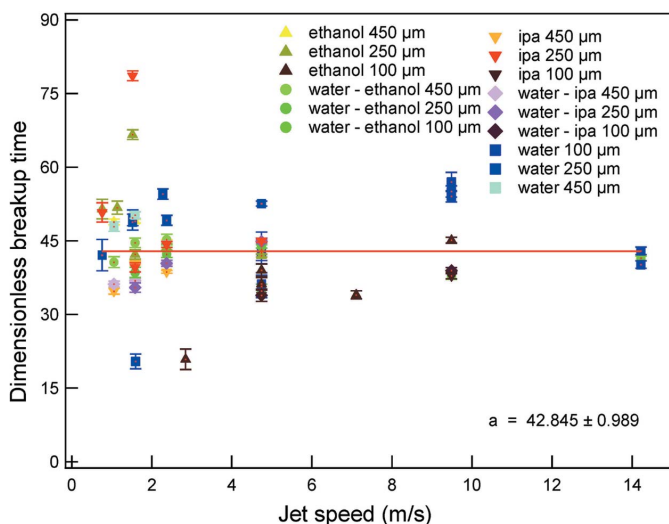


Figure 9 Dimensionless break-up time as a function of the jet speed at the nozzle exit for all the examined liquids in the Rayleigh regime. The line corresponds to the average of all values.

to determine the behaviour of the device used to produce the jet.

By applying *a posteriori* this estimation of the break-up time to the effect detected by Marmioli *et al.* (2010) for a jet with a diameter of 25 μm , we can attribute the change of integrated intensity at about 200 μs to the break-up of the liquid jet and not to the induction time of the reaction.

5. Conclusions

In the present paper it has been demonstrated that SAXS is a reliable and robust technique to detect and characterize liquid jet instability. It is not based on snapshots, as it is time and space averaged. This is particularly suited to studying droplets and surface instability. Moreover, thanks to its high spatial resolution, SAXS allows the observation of changes at the nanoscale level, where imaging cannot easily be performed. Unlike the techniques based on camera imaging, SAXS is not limited by the dimension of the jet in the micrometer or sub-micrometer range.

This ability to detect instability has important consequences for experiments based on liquid jets. In fact, due to their increasing use for studies of chemical and biological assays and reactions by means of SAXS and X-ray diffraction (both based on synchrotron radiation and FELs), it becomes essential to determine the behaviour of the liquid jet itself which acts as the sample carrier and is a non-negligible/major source of background signal. This is even more important in the case of liquid mixtures, which present complex behaviour. As every disturbance can cause an early break-up, and pumps and vibrations at the beamline give characteristic perturbations, tests for jet behaviour should be made before every measurement of samples or reactions with jets.

It has also been demonstrated that SAXS can be used for studying the mechanics of liquid microjets, by providing benchmark data for simulation and theory. In fact, the spatial scale of our experiments is at the border between the continuum scale and molecular dynamics. Our data can be employed for the description of liquid free jets ejected in still air. An estimate of the break-up time as a function of the characteristic time under such experimental conditions has also been given.

The authors wish to thank Michael Rappolt for useful discussions, Christian Morello for the precious technical support, and Dan Cojoc for advice and help with the high-resolution camera.

References

Amenitsch, H. (1992). PhD Thesis/Dissertation, pp. 1–122. Vienna, Austria.
 Amenitsch, H. & Marmioli, B. (2011). *Rend. Lincei*, **22**, S93–S107.
 Amenitsch, H., Rappolt, M., Kriechbaum, M., Mio, H., Laggner, P. & Bernstorff, S. (1998). *J. Synchrotron Rad.* **5**, 506–508.
 Boutet, S. *et al.* (2012). *Science*, **337**, 362–364.
 Chapman, H. N. *et al.* (2011). *Nature (London)*, **470**, 73–77.

Chu, K. & Thompson, A. R. (1962). *J. Chem. Eng. Data*, **7**, 358–360.
 David, G. & Pérez, J. (2009). *J. Appl. Cryst.* **42**, 892–900.
 Delteil, J., Vincent, S., Erriguible, A. & Subra-Paternault, P. (2011). *Comput. Fluids*, **50**, 10–23.
 Deponte, D. P., Doak, R. B., Hunter, M., Liu, Z., Weierstall, U. & Spence, J. C. H. (2009). *Micron*, **40**, 507–509.
 Deponte, D. P., McKeown, J. T., Weierstall, U., Doak, R. B. & Spence, J. C. (2011). *Ultramicroscopy*, **111**, 824–827.
 Eggers, J. & Villermaux, E. (2008). *Rep. Prog. Phys.* **71**, 1–79.
 El-Banna, M. M. & Ramadan, M. S. (1995). *J. Chem. Eng. Data*, **40**, 367–370.
 Feigin, L. A. & Svergun, D. I. (1987). *Structure Analysis by Small-Angle X-ray and Neutron Scattering*. New York/London: Plenum Press.
 Goldin, M., Yerushalmi, J., Pfeffer, R. & Shinnar, R. (1969). *J. Fluid Mech.* **38**, 689.
 Haberkorn, H., Franke, D., Frechen, T., Goesele, W. & Rieger, J. (2003). *J. Colloids Int. Sci.* **259**, 112–126.
 Hammersley, P. (1998). *Fit2D Reference Manual V3.1*. Internal Report ESRF98HA01T. ESRF, Grenoble, France.
 Hentschel, M. P., Hosemann, R., Lange, A., Uther, B. & Brückner, R. (1987). *Acta Cryst.* **A43**, 506–513.
 Hoeve, W. van, Gekle, S., Snoeijer, J. H., Versluis, M., Brenner, M. P. & Lohse, D. (2010). *Phys. Fluids*, **22**, 1–11.
 Homer, C. J., Jiang, X., Ward, T. L., Brinker, C. J. & Reid, J. P. (2009). *Phys. Chem. Chem. Phys.* **11**, 7780–7791.
 Innocenzi, P., Malfatti, L., Costacurta, S., Kidchob, T., Piccinini, M. & Marcelli, A. (2008). *J. Phys. Chem. A*, **112**, 6512–6516.
 Kalaaji, A., Lopez, B., Attané, P. & Soucemarianadin, A. (2003). *Phys. Fluids*, **15**, 2469.
 Lange, K. M., Könnicke, R., Ghadimi, S., Golnak, R., Soldatov, M. A., Hodeck, K. F., Soldatov, A. & Aziz, E. F. (2010). *Chem. Phys.* **377**, 1–5.
 Lin, S. P. & Reitz, R. D. (1998). *Annu. Rev. Fluid Mech.* **30**, 85–105.
 Lu, Y., Yang, Y., Sellinger, A., Lu, M., Huang, J., Fan, H., Haddad, R., Lopez, G., Burns, A. R., Sasaki, D. Y., Shelnett, J. & Brinker, C. J. (2001). *Nature (London)*, **410**, 913–917.
 Marmioli, B., Greci, G., Cacho-Nerin, F., Sartori, B., Ferrari, E., Laggner, P., Businaro, L. & Amenitsch, H. (2009). *Lab Chip*, **9**, 2063–2069.
 Marmioli, B., Greci, G., Cacho-Nerin, F., Sartori, B., Laggner, P., Businaro, L. & Amenitsch, H. (2010). *Nucl. Instrum. Methods Phys. Res. B*, **268**, 329–333.
 Pires, R. M., Costa, H. F., Ferreira, A. G. M. & Fonseca, I. M. A. (2007). *J. Chem. Eng. Data*, **52**, 1240–1245.
 Plomp, J., Barker, J. G., de Haan, V. O., Bouwman, W. G. & van Well, A. A. (2007). *Nucl. Instrum. Methods Phys. Res. A*, **574**, 324–329.
 Polte, J., Erler, R., Thuenemann, A. F., Sokolov, S., Ahner, T. T., Rademann, K., Emmerling, F. & Kraehnert, R. (2010). *ACS Nano*, **4**, 1076–1082.
 Porod, G. (1952). *Kolloid Z.* **125**, 51–57.
 Priebe, M., Kalbfleisch, S., Tolkiehn, M., Köster, S., Abel, B., Davies, R. J. & Salditt, T. (2010). *New J. Phys.* **12**, 1–12.
 Rayleigh, L. (1879). *Proc. R. Soc. London*, **29**, 71–97.
 Redecke, L. *et al.* (2013). *Science*, **339**, 227–230.
 Sander, W. & Weigand, B. (2008). *Phys. Fluids*, **20**, 1–18.
 Schmidt, W., Bussian, P., Lindén, M., Amenitsch, H., Agren, P., Tiemann, M. & Schüth, F. (2010). *J. Am. Chem. Soc.* **132**, 6822–6826.
 Shapiro, D. A., Chapman, H. N., DePonte, D., Doak, R. B., Fromme, P., Hembree, G., Hunter, M., Marchesini, S., Schmidt, K., Spence, J., Starodub, D. & Weierstall, U. (2008). *J. Synchrotron Rad.* **15**, 593–599.
 Spence, J. C. H., Weierstall, U. & Chapman, H. N. (2012). *Rep. Prog. Phys.* **75**, 102601.

- Stengel, F., Aebersold, R. & Robinson, C. V. (2012). *Mol. Cell Proteomics*, **11**, 1–13.
- Suzuki, T. (2012). *Int. Rev. Phys. Chem.* **31**, 265–318.
- Tolan, M. (1999). *X-ray Scattering from Soft-Matter Thin Films*. Berlin, Heidelberg, New York: Springer-Verlag.
- Vazquez, G., Alvarez, E. & Navaza, J. M. (1995). *J. Chem. Eng. Data*, **40**, 611–614.
- Walker, J. R. (2012). PhD Thesis/Dissertation, pp. 1–163. University of Maryland, USA.
- Walker, J. R. & Calabrese, R. V. (2011). *Can. J. Chem. Eng.* **89**, 1096–1103.
- Wilson, K. R., Schaller, R. D., Co, D. T., Saykally, R. J., Rude, B. S., Catalano, T. & Bozek, J. D. (2002). *J. Chem. Phys.* **117**, 7738.